PLD-Assisted VLS Growth of Aligned Ferrite Nanorods, Nanowires, and Nanobelts−Synthesis, and Properties

Jenny Ruth Morber,[†] **Yong Ding,**[†] **Michael Stephan Haluska,**[†] **Yang Li,**[‡] **J. Ping Liu,**[‡]
Zhong Lin Wang,*,[†] **and Robert L. Snyder*,**[†]

School of Materials Science and Engineering, Georgia Institute of Technology, Atlanta, Georgia 30332-0245,
and Department of Physics, University of Texas at Arlington, Arlington, Texas 76019

We report here a systematic synthesis and characterization of aligned α-Fe$_2$O$_3$ (hematite), ε-Fe$_2$O$_3$, and Fe$_3$O$_4$ (magnetite) nanorods, nanobelts, and nanowires on alumina substrates using a pulsed laser deposition (PLD) method. The presence of spherical gold catalyst particles at the tips of the nanostructures indicates selective growth via the vapor−liquid−solid (VLS) mechanism. Through a series of experiments, we have produced a primitive "phase diagram" for growing these structures based on several designed pressure and temperature parameters. Transmission electron microscopy (TEM) analysis has shown that the rods, wires, and belts are single-crystalline and grow along $\langle 111 \rangle_m$ or $\langle 110 \rangle_h$ directions. X-ray diffraction (XRD) measurements confirm phase and structural analysis. Superconducting quantum interference device (SQUID) measurements show that the iron oxide structures exhibit interesting magnetic behavior, particularly at room temperature. This work is the first known report of magnetite 1D nanostructure growth via the vapor−liquid−solid (VLS) mechanism without using a template, as well as the first known synthesis of long ε-Fe$_2$O$_3$ nanobelts and nanowires.

1. Introduction

Advances in growth and characterization techniques have led to the production of modern magnetic materials which reveal a range of fascinating phenomena. These phenomena are derived from the advantages of the spin component of electrons in addition to charge, providing an extra level of complexity in physics and an extra degree of freedom in device design. In the nanoscale, where the influence of surface effects is much enhanced, novel properties, such as increased magnetization or superparamagnetism, are often observed.[1] Properties of single nanostructures can be tailored to specific needs by varying size, composition, or growth morphology. For arrays of nanowires, spatial control and alignment with respect to the substrate are critical for integration into electronic and photonic technologies.[2] Single-crystalline structures are also essential since the presence of grains and grain boundaries will affect magnetic domain structure and electron transport such that a polycrystalline nanowire behaves more like an aggregated chain of particles rather than a true one-dimensional (1D) nanostructure.

Nanoscale magnetic ferrites are of particular interest due to their size and chemical compatibility with biological tissues and their unique combination of electronic and magnetic properties. In bulk, magnetite (Fe$_3$O$_4$) has a high Curie temperature ($T_c \sim$ 850 K) and nearly full spin polarization at room temperature,[3] which make it appealing for giant magnetoresistance and spin valve devices. Current biomedical applications of magnetite nanoparticles include targeted drug delivery,[4,5] ultra-sensitive bio-agent detection,[6,7] gene therapy,[4,8] hyperthermic cancer treatment,[4,5,9] and magnetic resonance imaging (MRI) contrast enhancement.[4,10,11] The stability and electronic properties of the more common hematite (α-Fe$_2$O$_3$) make it an ideal candidate as a photocatalyst and as a photoelectrode in solar energy conversion applications.[12]

Much work is also focused on developing ferrite nanoparticles for ultrahigh density memory storage[13,14] and advanced communications devices.[15] Ferrite nanoscale materials are favored over other rare-earth alloys to aid in addressing the current need to overcome superparamagnetic limits in conventional recording due to their relatively low cost, stability, low toxicity, and most importantly, high resistivity, reducing unfavorable eddy current energy loss.[16] ε-Fe$_2$O$_3$ is well suited to such applications due it its very high room temperature coercivity (maximum H_c = 20 kOe).[16,17] In fact, at low magnetic saturation (M_s), nanorods of ε-Fe$_2$O$_3$ exhibit greater coercivity than "model" hard magnetic materials, such as barium hexaferrite and HCP Co.[18] Unlike α-Fe$_2$O$_3$, ε-Fe$_2$O$_3$ is considered a rare and metastable form of iron oxide[19] and, until now, has only been observed in small nanorods or nanoparticles. It is ferrimagnetic at room temperature ($T_c \sim$ 510 K), and due to its magnetic moment coupled with an orthorhombic non-centrosymmetric structure, ε-Fe$_2$O$_3$ is expected to also exhibit piezoelectric, magnetoelectric, optical, and pyroelectric behaviors. Such coupling of spontaneous magnetization and electronic polarization promises exciting advances in such areas as electric/magnetic field tunable devices or multiple state memory.[20]

Still, many current or proposed applications that utilize ferrite nanoparticles require a set of properties not achievable through available particle sizes and morphologies.[21,22] Current technologies relying on magnetic iron oxide particles or quantum dots could be greatly improved through enhanced magnetic and electronic properties. On the basis of experiments showing large variation in magnetic behavior due to size or morphology differences in nanoparticles as well as a few recent studies on

* Corresponding authors. E-mail: bob.snyder@mse.gatech.edu (R.L.S.); zhong.wang@mse.gatech.edu (Z.L.W.).
† Georgia Institute of Technology.
‡ University of Texas at Arlington.

Growth of Ferrite Nanorods, Nanowires, and Nanobelts

J. Phys. Chem. B, Vol. 110, No. 43, 2006 **21673**

ferrite nanorods and nanowires, 1D nanostructured ferrites are expected to exhibit many properties unlike those of particles of the same phase.[23−26] Recent research has shown that the high aspect ratio of magnetic nanowires can produce a larger magnetic moment than that observed in particles of the same volume, providing significant benefits in numerous applications.[27] Biomedical applications, for example, could potentially benefit greatly through the use of such nanostructures, allowing advances both in the lab and in the clinical setting. In fields such as local drug delivery, improved magnetic properties would allow the ability to deliver drugs more quickly and accurately, enabling treatment of smaller areas with lower dosages and decreased side effects. Novel ferrite properties could likewise benefit current communications, defense, memory storage, and energy technologies, among others. The large coercivity (H_c) observed in nanoparticles of ϵ-Fe_2O_3, for example, is believed to be the result of the material's large magnetocrystalline anisotropy.[16,17] One-dimensional morphologies provide an additional component of magnetic anisotropy, the shape anisotropy.[28] Often dominant in nanoscale materials, shape anisotropy contributions could produce 1D structures of ϵ-Fe_2O_3 capable of properties far exceeding those observed in nanoparticle morphologies. One-dimensional nanostructures of magnetite, hematite, and ϵ-Fe_2O_3 also provide ideal theoretical systems for fundamental studies of electron spin and magnetic behavior of materials near quantum levels. Magnetic characterization of 1D ferrite nanostructures is essential both as a step toward exploitation of desirable properties for new and improved applications and also as a means to better understand electronic behavior in the nanoscale regime.

Although iron oxide nanowires and nanorods have been fabricated through a variety of methods, such as templating,[25,29] hydrothermal synthesis,[30] thermal decomposition,[31] and sol−gel[16,17,20] techniques, these methods are often plagued by undesired contaminants, lack of control over morphology, size, and orientation, grainy structures, and the need for annealing treatments post-synthesis.[29,32] Oxidation of iron has been used to produce arrays of α-Fe_2O_3 nanowires;[2] however, this method does not allow for location-specific selection of nanowire growth. Controllable vapor deposition processes are promising candidates for scalable industrial production in the future, due to their simplicity and low cost, and have been employed to overcome many of these obstacles in simple chemical systems, such as ZnO,[33,34] ZnS,[35,36] and CdSe,[37,38] yet evaporative methods in the synthesis of iron oxide 1D nanostructures have produced limited success. Magnetite nanowire fabrication, in particular, has proven difficult due to the thermodynamic driving force for crystallization of vapors into the more stable α-Fe_2O_3 phase. The PLD method has shown some recent success in magnetite synthesis, however, only with the aid of a template, necessitating fabrication of either core/shell or tube-like structures.[29,39] In addition, ϵ-Fe_2O_3 has until now been observed only in nanoparticle and short nanorod morphologies, regardless of method. PLD-assisted VLS growth, such as that reported for the first time here, allows for simple synthesis of hematite and magnetite 1D nanostructure arrays and long ϵ-Fe_2O_3 nanobelts, lacking many of the problems encountered with other methods, while still granting spatial and size control.

The PLD method allows an additional level of control to the researcher due to the ability to maintain stoichiometry defined by a premixed target material. The ability of PLD to retain the target stoichiometry in the deposited structure is the result of the extremely high heating rate of the target surface (∼108 K/s) due to the pulsed laser irradiation. This leads to the congruent
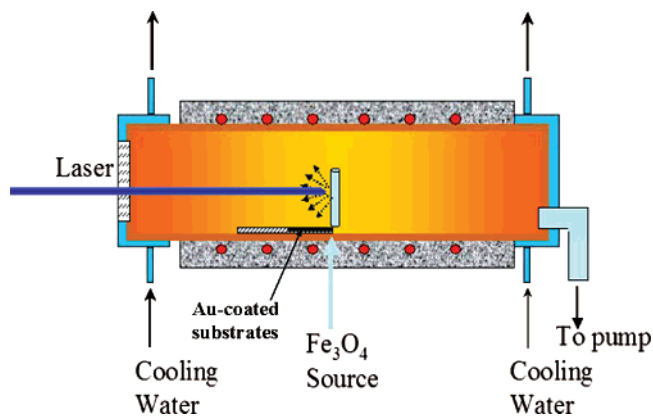

Figure 1. Schematic showing PLD synthesis apparatus. Laser energy is directed through a treated glass window to a pressed magnetite target. Vapors are released and re-condensed as 1D nanostructures nucleated on gold catalyst particles.

evaporation of the target irrespective of the evaporating point of the constituent elements or compounds of the target. Also, because of the high heating rate of the ablated materials, laser deposition demands a much lower substrate temperature than other evaporation growth techniques.[40] Despite the degree of control granted by the PLD method, to date, literature has not previously reported synthesis of single-crystalline magnetite nanowires or nanobelts via evaporation methods without the aid of a template.

In this paper, we have successfully applied the PLD-assisted method for growth of aligned hematite and magnetite nanorods, nanobelts, and nanowires. We have also achieved by this method the first known synthesis of ϵ-Fe_2O_3 long nanobelts. Through a series of experiments, we have produced a primitive "phase diagram" for growing these structures based on several designed pressure and temperature parameters. This work is the first known report of magnetite 1D nanostructure growth via the vapor−liquid−solid (VLS) mechanism without using a template. The structure of the nanowires has been investigated by transmission electron microscopy (TEM) and X-ray diffraction (XRD). The magnetic properties of the synthesized nanostructures have been investigated by superconducting quantum interference device (SQUID).

2. Experimental Method

The iron oxide nanorods, nanowires, and nanobelts were synthesized via pulsed laser deposition (PLD), using a pellet of pressed magnetite powder as target. Approximately 5 g of Fe_3O_4 powder (Alfa Aesar 98%) was pressed in a 9.5 mm diameter steel die at ∼680 kg pressure to form a cylindrical pellet. The Fe_3O_4 target was placed in a quartz tube in the center of a single-zone horizontal tube furnace. A schematic of the basic apparatus is shown in Figure 1. Next to the target was placed a quartz boat containing polycrystalline alumina wafer substrates coated with 2 nm of Au film to form catalyst islands. The tube ends were closed and water-cooled to maintain a uniform thermal gradient, with one end connected to a rotary vacuum pump and the other to a gas supply. To minimize residual oxygen, the tube was evacuated to 10^{-2} mbar and held for 1 h prior to running the experiment. Argon gas (99.999%) was intermittently added during this time at a flow rate of 50 sccm to facilitate reduction of adsorbed oxygen and then stopped to allow the system to return to a low pressure of around 0.02 mbar. The furnace was then allowed to heat up at a rate of 20 °C/min to the desired maximum temperature under a well-maintained ambient pressure prescribed according to the chart
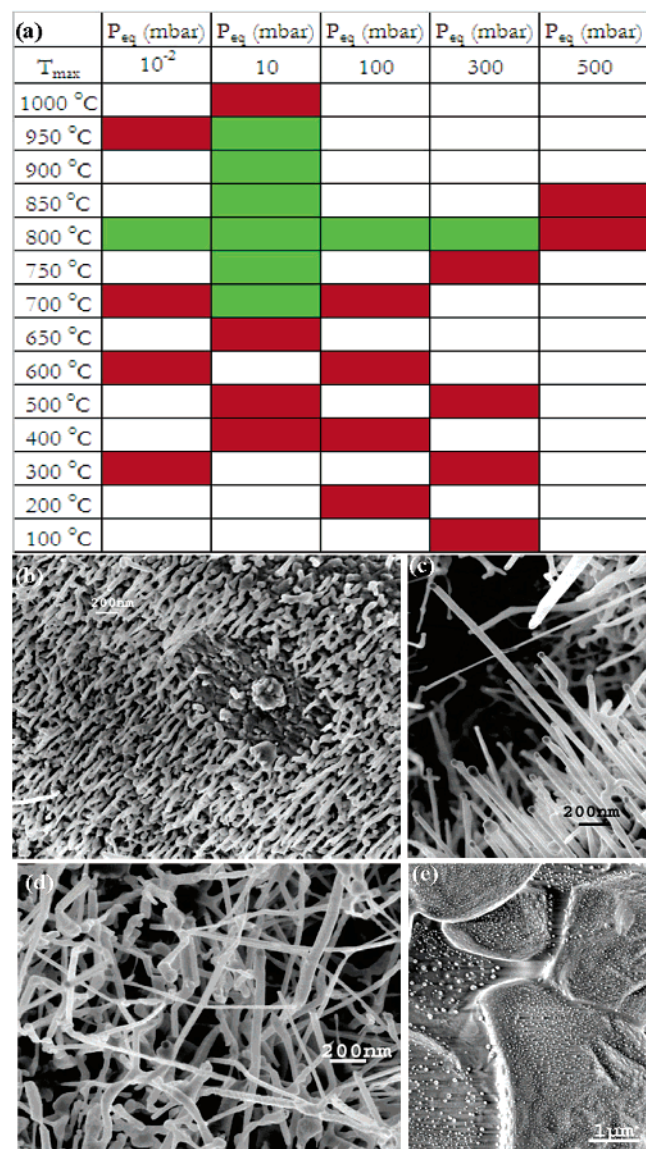
(a)

T_{max}	P_{eq} (mbar) 10^{-2}	P_{eq} (mbar) 10	P_{eq} (mbar) 100	P_{eq} (mbar) 300	P_{eq} (mbar) 500
1000 °C		green			
950 °C	red	green			
900 °C		green			
850 °C		green			red
800 °C	green	green	green	green	red
750 °C		green		red	
700 °C	red	green	red		
650 °C		red			
600 °C	red		red	red	
500 °C		red		red	
400 °C		red	red		
300 °C	red			red	
200 °C			red	red	
100 °C				red	

Figure 2. (a) Table showing tested pressure/temperature combinations and observed outcomes. Each cell represents a unique experiment. Green cells indicate combinations that produced high-density 1D nanowire growth. Red cells indicate no or very low growth. White cells indicate untested parameter combinations or those in which results were inconclusive. All other parameters were kept constant in these experiments. (b) SEM image showing short rods synthesized at 700 °C, 10 mbar. (c) SEM image showing long belts synthesized at 900 °C, 10 mbar. (d) SEM image displaying greater secondary growth after 120 min of laser energy exposure compared to usual 60 min growth time at 900 °C, 10 mbar. (e) SEM image showing no 1D growth at 900 °C, 10 mbar, without laser energy.

shown in Figure 2a. Argon flow gas was simultaneously introduced into the system at 50 sccm and was maintained throughout the duration of the synthesis.

Once the temperature and pressure had stabilized, pulsed laser energy generated by a Compendex series excimer 102 laser (20 Hz, 30 kV, ~300 mJ) was directed through a transparent window on one end of the tube and focused toward the source material placed in the beam path. The laser spot on the target measured approximately 1 mm wide by 5 mm long in most experiments. The laser was then allowed to ablate the target for 60 min, while pressure and temperature remained constant. After 60 min, the laser, furnace, and flow gas were turned off, and the system was evacuated back down to 0.02 mbar. A fan was placed near the tube to ensure rapid cooling. After the

system reached room temperature, nitrogen gas was pumped into the tube to equilibrate the pressure, the tube was opened, and the substrate with the deposited sample was carefully collected and loaded onto an SEM stub for analysis. It was noted that most samples appeared red/orange to gray in color with rainbow-like fringes on the substrate radiating away from the leading edge.

The as-synthesized sample was directly imaged using a LEO 1530 field emission scanning electron microscope (SEM) with a resolution of 1 nm. The accelerating beam voltage was limited to 3 kV to reduce sample charging and potential damage. Some nanobelts were observed to interact with the electron beam, occasionally vibrating and later breaking if under beam focus. Several images as well as EDS data on the sample were collected.

Grazing incidence X-ray diffraction measurements were performed on each sample using a PANalytical X-Pert Pro MRD with Cu Kα radiation. A 1° grazing angle was used to minimize substrate signal noise, along with a parabolic mirror, 0.27° parallel plate collimator with a flat graphite crystal diffracted beam monochromator. The monochromator was utilized to reduce iron fluorescence under Cu radiation. Measurements were taken with a tube power of 45 kV and 40 mA, from 28 to 60° 2θ, with a 0.04° 2θ step size and a 100 s count time.

For detailed local structural analysis, a carbon film coated copper grid was swept over the sample and loaded into an JEOL 4000EX high-resolution transmission electron microscope (TEM) operating at 400 kV. Electron diffraction patterns as well as high-resolution images of several nanostructures were recorded and developed on film. EDS coupled with a Hitachi HF-2000 (FEG) TEM provided further evidence for chemical identification of the sample.

3. Results and Discussion

3.1. Systematic Synthesis Study. To better understand the conditions necessary for 1D nanostructure growth using the VLS-assisted PLD method, we undertook a series of experiments in which nanostructure growth was correlated to systematic variations in experimental parameters. As Figure 2a shows, the parameters most explored were the maximum ambient temperature (T_{max}) inside the tube and the controlled equilibrium pressure (P_{eq}) during laser ablation. Each cell in the table represents a possible unique experiment keeping all other variables, such as substrate type, catalyst density, target species, Ar flow rate, temperature ramp rate, ablation time, laser energy, and laser frequency, constant. After each experiment was complete, samples were examined in the SEM to determine the ability of the chosen parameters to sustain growth of 1D ferrite nanostructures. In the figure, red cells correspond to experiments in which nanowire growth was unsuccessful, green cells correspond to parameters yielding successful growth, and white cells correspond to untested parameter combinations, or those in which results were inconclusive.

Since the ferrite nanostructures grew only on catalyst particles, successful growth was measured primarily according to nanostructure length rather than density. For the purposes of this study, a successful experiment was defined as one showing uniform high-density growth of nanostructures with length dimensions at least 3 times that of the catalyst particle diameter. In fact, the smallest nanorods found in these experiments displayed lengths far greater than the minimum described. The best 1D ferrite nanostructure growth was reliably found to occur from 700 to 950 °C at 10 mbar pressure. Experiments utilizing these parameters were repeated several times with consistent

Growth of Ferrite Nanorods, Nanowires, and Nanobelts

J. Phys. Chem. B, Vol. 110, No. 43, 2006 **21675**

results. Figure 2b and c shows length variation of nanostructures according to chamber temperature (T_{max}) at time of synthesis. Nanorods grown at 700 °C, as shown in Figure 2b, were aligned, and single-crystalline ones, just like those shown in Figure 2c, grown at 900 °C, with the only difference being nanostructure length. This result illustrates our ability to control ferrite nanostructure size simply by varying reaction chamber temperature.

Although P_{eq} and T_{max} were the primary parameters investigated in this study, we also examined the effect of laser ablation time on 1D nanoferrite growth. Results of experiments carried out at 900 °C and 10 mbar showed that increasing ablation time from 60 to 90 or 120 min did not significantly increase mean nanostructure length, but instead increased branching and secondary growth in the sample. Figure 2d demonstrates this finding with an SEM image taken from a sample ablated for 120 min at 900 °C, 10 mbar, the same P_{eq} and T_{max} combination shown in Figure 2c after the normal 60 min ablation time. We were also curious to test our hypothesis that the laser energy is the primary energy source for nanowire growth, and whether instead T_{max} was producing growth before or in addition to the target's exposure to laser energy. To answer this question, we conducted an experiment in which the procedure was followed exactly as in other runs; however, the target was not exposed to laser energy. This experiment was conducted at 10 mbar, 900 °C, a parameter combination previously shown to produce very high density ferrite nanostructures when laser energy was applied. The results of this test are shown in Figure 2e. Clearly, there is no growth at all on the substrate, confirming our hypothesis that the laser irradiation is the principle energy source responsible for target vaporization and resulting nanostructure growth. This result also indicates the ability for greater control over growth time in the PLD process relative to thermally driven vapor evaporation growth techniques in which critical growth initiation temperature is often unknown.

3.2. Electron Microscope Characterization of Magnetite and Hematite Nanostructures. Figure 3 shows typical SEM images recorded from an as-synthesized sample with the inset containing EDS data gathered from TEM. The EDS data taken from TEM analysis indicate the presence of Fe, Mg, and O, with Cu and C radiation originating from the sample grid, and Si peaks due to the signature of the detector. We were able to grow both Mg-doped and pure ferrite nanostructures via this method. Images in Figure 3a,b illustrates ferrite nanowires, including some nanobelts with approximately 6 atom % Mg present, while Figure 3c,d shows pure iron oxide nanostructures. As these images demonstrate, both pure and Mg-doped 1D ferrites are of high-quality single-crystalline nanostructures. Mg incorporation seems to occur almost exclusively in the longest nanobelts. Nanowires and nanobelts in Figure 3 were grown at a maximum ambient temperature of 900 °C. Although nanostructure dimensions varied greatly within samples, nanowires and nanobelts grown at 900 °C were generally highly dense, and on the order of 1 μm long $\times$ 30 nm wide, with the longest nanowires growing up to approximately 5 μm. Most long structures appeared to possess a rectangular cross section, giving them a belt-like morphology; however, those with more circular cross section were observed, as well, especially at the higher temperatures. Under the 700 °C condition, nanorods were the prevalent morphology with typical dimensions of 500 nm long $\times$ 30 nm wide. Long nanobelts up to 7 microns in length and averaging around 100 nm in width were observed under both temperature conditions and appeared to grow in random
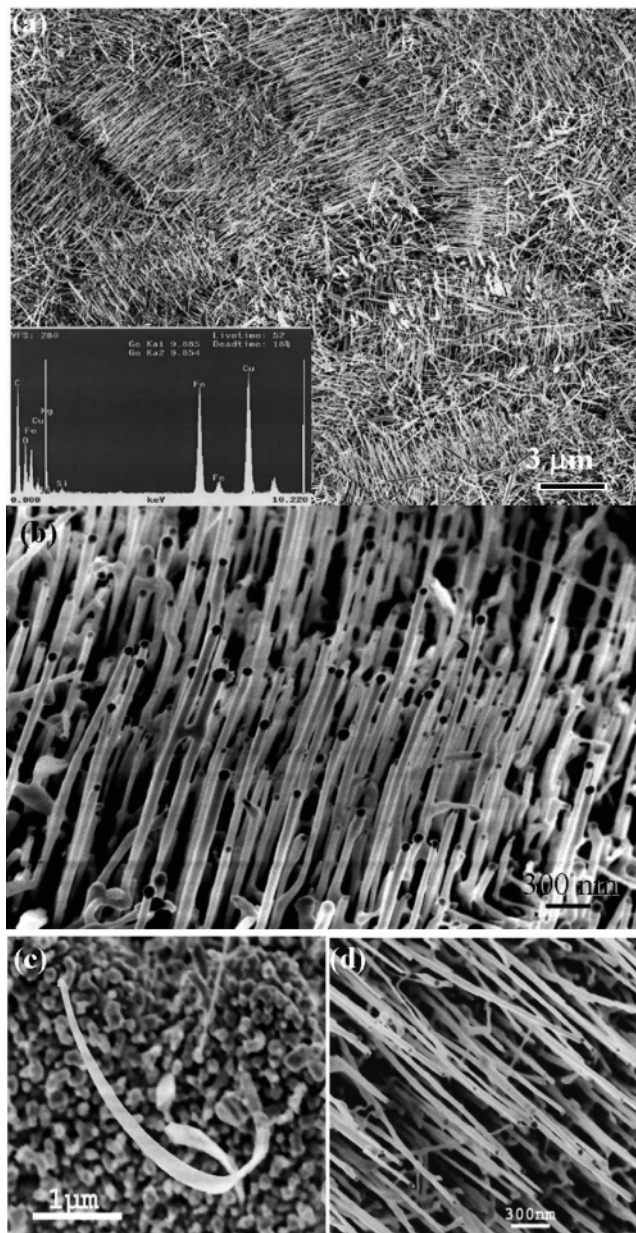

Figure 3. SEM images of Mg-doped and pure iron oxide 1D nanostructures. (a) Low-magnification SEM image of aligned iron oxide nanowires doped with Mg showing local alignment along alumina crystallites. Inset shows EDS chemical signature. (b) Higher magnification SEM image showing aligned Mg-doped iron oxide nanorods. (c) SEM image showing long nanobelt structure most likely having ϵ-Fe$_2$O$_3$ microstructure, without presence of Mg. (d) SEM image showing group of aligned iron oxide nanowires with Mg absent.

orientations in or near grain boundaries. Density of these structures likewise increased at elevated temperature.

Note the uniform length and alignment of the nanorods localized on different alumina grains as seen at low magnification in Figure 3a. Interestingly, each grain promotes aligned growth in a specific direction relative to the plane of the substrate. It appears that some grain faces are more favorable and initiated growth earlier, as nanostructures are longer in some orientations relative to others. This effect is not due to simple vapor flow variation as evidenced by the observation that nanostructures growing on adjacent grains commonly exhibited significant length differences. The nanostructures' preference to grow at specific orientations and according to substrate crystallography indicates that researchers should be able to
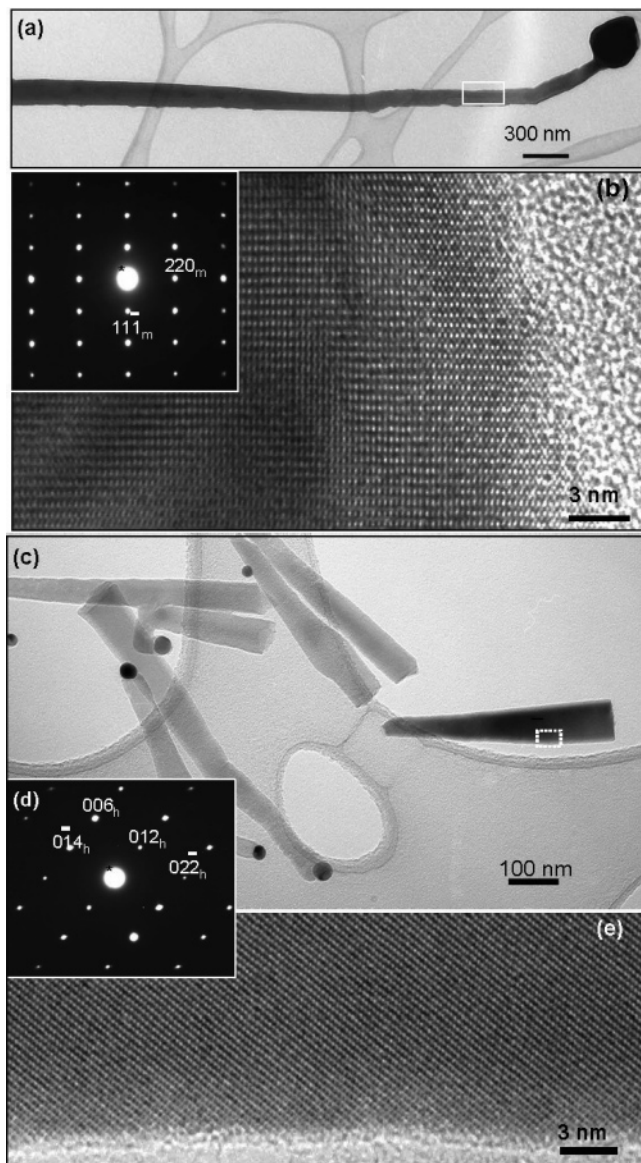
Figure 4. TEM data on magnetite and hematite nanostructures. (a) Low-magnification bright field TEM image of magnetite nanowire. (b) High-resolution TEM image of nanowire taken from the side edge of the wire in (a), illustrating high-quality single-crystalline nature of the wire. (c) Low-magnification bright field TEM image of hematite nanorods with Au particle tips. (d) Electron diffraction image taken from dark rod in previous image shows single-crystalline nature of the rod. (e) High-magnification TEM image of the section outlined in (c), showing well ordered structure and very little amorphous material on the nanorod surface.

exactly control the angle of growing nanostructures relative to the substrate by carefully engineering surface orientation on single-crystalline substrates. In fact, later synthesis on *c*-plane and *a*-plane sapphire (single-crystalline Al_2O_3) produced high density arrays with perpendicular and in-plane growth, respectively. Figure 3b also clearly shows each nanowire tip terminated with a spherical gold particle. The ability to determine nanowire location through precise placement of catalyst material provides further spatial control over the nanowire synthesis.

Figure 3c is a typical image of the frequently observed long nanobelts found in our samples. Electron diffraction analysis (not shown) as well as XRD data indicate that these long nanobelts exhibit an ϵ-Fe_2O_3 phase of iron oxide. Some were shown in EDS to contain a small amount of Mg species as mentioned previously. Mg incorporation into these nanobelts
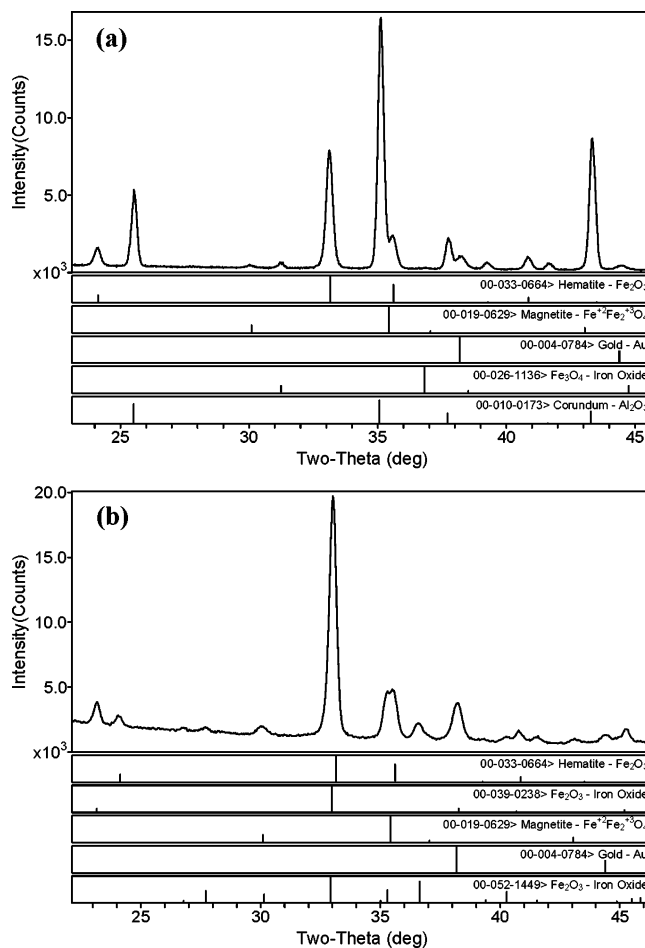

Figure 5. XRD data taken from samples grown at 800 °C, 10 mbar, and 750 °C 10 mbar, respectively. (a) XRD signal from grazing incidence measurements of iron oxide nanobelts and nanowires grown on polycrystalline alumina. (b) Similar measurements on iron oxide nanostructures grown on a *c*-plane sapphire substrate.

is not surprising given reports that addition of column II cations, such as Sr^{2+} or Ba^{2+}, to ϵ-Fe_2O_3 stabilized the phase and allowed for growth of larger nanocrystals.[16,17] In our samples, EDS analysis did not reveal Mg in all long ϵ-Fe_2O_3 nanobelts, indicating that its presence is not necessary for ϵ-Fe_2O_3 nanobelt formation using this method.

Figure 4a–e shows TEM data of magnetite and hematite nanowires. Both hematite and magnetite nanostructures were found within the same sample, with no observable local phase domains. Although early samples were shown to contain a majority of hematite structures, predominantly magnetite samples were later synthesized by flowing Ar (50 sccm) for 10–20 min intervals during initial tube evacuation to better eliminate residual oxygen in the system. Adding a piece of iron foil to the chamber to act as an oxygen "getter" was also helpful in increasing the relative magnetite yield. This finding indicates that phase can be controlled through careful variation of oxygen partial pressure within the tube. In Figure 4a, one can see a bright field image of a magnetite nanowire with the spherical gold catalyst particle visible at the tip. The high-resolution TEM image of this structure seen in Figure 4b illustrates the near perfect single-crystalline arrangement of atoms in the nanowire. Very little amorphous material is present on the surface. The electron diffraction pattern in the inset provides further evidence for the single-crystalline nature of this nanowire and shows that the wire grew along the [1$\bar{1}$1] direction. This is not the sole growth direction of magnetite nanowires in the sample, as others
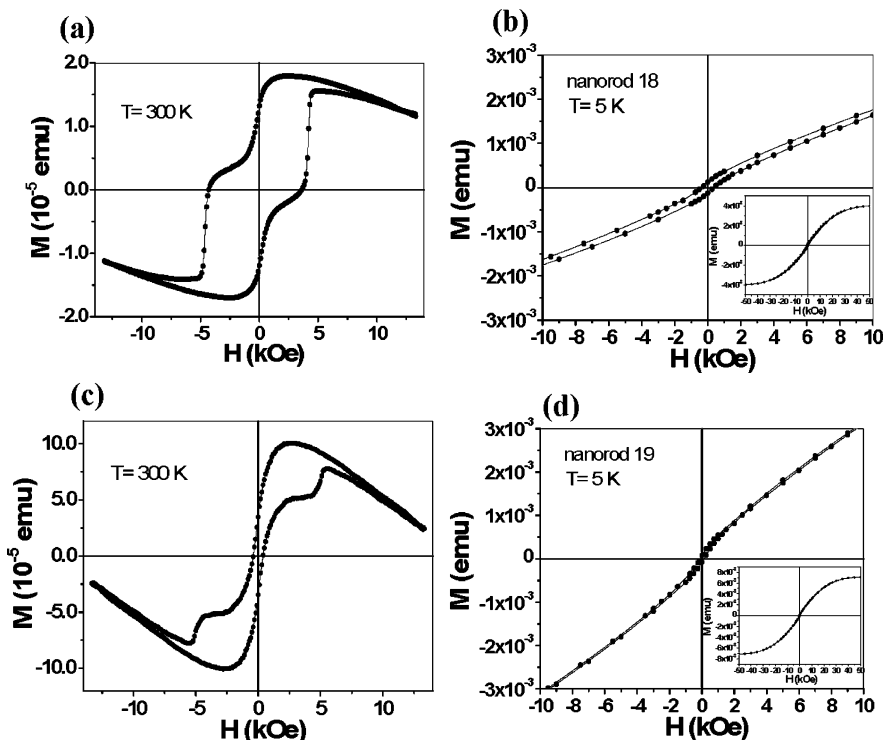
Figure 6. Magnetic hysteresis behavior of iron oxide nanostructures grown at 700 °C, measured with SQUID. (a) $M-H$ loop at 300 K showing ferromagnetic behavior and wasp-waist shape most likely derived from multiphase nature of the sample. (b) $M-H$ loop at 5 K with low-field region expanded, showing soft magnetic behavior. Right inset: $M-H$ loop from -5 to 5 T. (c and d) Similar results in a sample prepared at 900 °C. In (c), the presence of the soft phase is more pronounced, consistent with observations of increased hematite concentration in this sample.

characterized by TEM (not shown) were found to grow along the $\langle 110 \rangle$ directions.

Presence of magnetite rather than maghemite (γ-Fe$_2$O$_3$ defect spinel) in the samples was confirmed through careful determination of lattice parameters from TEM diffraction data as well as XRD phase analysis. Both electron diffraction and XRD can distinguish the structures based on differences in the space groups exhibited by each structure, with Fe$_3$O$_4$ and γ-Fe$_2$O$_3$ corresponding to $Fd3m$ (227) and $P4_232$ (208), respectively. The d spacing of Fe$_3$O$_4$ is about 0.48 nm, while that of γ-Fe$_2$O$_3$ should be 0.59 nm.

Figure 4c shows a bright field TEM image of several hematite nanorods. Again, Au catalyst particles are observed at the tips, indicating VLS as the dominant growth mechanism in the sample. The high-resolution image in Figure 4e clearly shows the ordered arrangement of atoms and the lack of a significant amorphous layer at the surface. The nanorod in this figure grew along the $[01\bar{1}]$ direction as seen in the electron diffraction pattern shown in Figure 4d.

3.3. XRD Characterization of Ferrite Nanostructures. X-ray diffraction characterization of several samples is given in Figure 5. The image in Figure 5a shows XRD data from a sample grown at 700 °C, 10 mbar, on a polycrystalline alumina substrate. The diffraction pattern was analyzed with Jade software. Although the polycrystalline alumina peaks are predictably the strongest, the pattern clearly shows the presence of gold, magnetite, and hematite, confirming our assessment though electron diffraction studies. Figure 5b shows a similar pattern performed on an iron oxide nanowire sample grown at 750 °C, 10 mbar, on a c-plane sapphire substrate. Sapphire was used in this example to eliminate the influence of the substrate on the XRD diffraction pattern. The structures in this sample grew primarily perpendicular to the substrate in a high-density nanowire array tipped with gold particles. Phase identification of the diffraction pattern in Figure 5b using MDI Jade7.5 yields

five known phases: Au (PDF#4$-$784), hematite (Fe$_2$O$_3$ PDF#33$-$664), a magnetite-like phase (closest match PDF#19$-$629), an orthorhombic iron oxide (Fe$_2$O$_3$ PDF#52$-$1449) found to correspond to ϵ-Fe$_2$O$_3$, and a cubic iron oxide (Fe$_2$O$_3$ PDF#39$-$238). The cubic iron oxide phase has been identified as a BCC phase. Since the current paper focuses on the physical chemistry involved in the synthesis, detailed structure analysis of the new phase will be presented elsewhere.

Quantitative analysis performed using the reference intensity ratio (RIR) method on a similar sample yields a weight fraction ratio of 0.57 hematite to magnetite. It should be noted that previous XRD analysis of the clean alumina substrate (not shown) indicates small amounts of a spinel aluminum oxide phase within the corundum Al$_2$O$_3$ wafer. Most likely, this is a MgAl$_2$O$_4$ phase added to aid in sintering and is the source of the Mg seen in some of our long nanobelt structures.

3.4. SQUID Characterization of Ferrite Nanostructures. SQUID (superconducting quantum interference device) measurements on samples created at 700 °C, 10 mbar, and 900 °C, 10 mbar, are shown in Figures 6 and 7, respectively. Figure 6 demonstrates magnetic hysteresis behaviors of these samples at 300 K (room temperature) and 5 K. Data for nanostructures created under the 700 °C condition are shown in Figure 6a,b, with Figure 6c,d correlating to the 900 °C synthesized sample. As shown in Figure 6a, the nanostructures grown at 700 °C exhibit strong ferromagnetic behavior at room temperature. The kink, or "wasp waist", shown at approximately 4 kOe in the curve indicates presence of two compatible magnetic phases. The diamagnetic nature of the alumina substrate is most likely the cause of the curve's decay at high field strengths. While ferromagnetic behavior of the kind shown here is expected for the magnetite 1D nanostructures, above the Morin temperature of hematite ($\sim$263 K bulk), magnetic moments are canted slightly away from the antiferromagnetic axis, resulting only in a very small net positive magnetization. This effect should
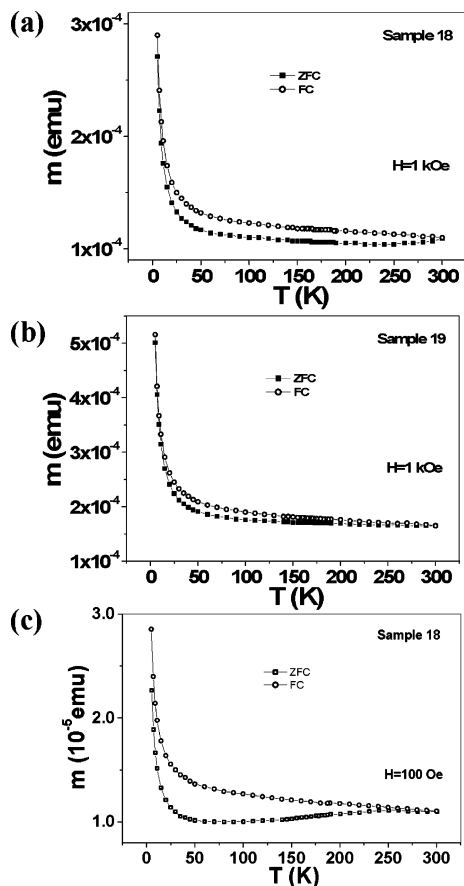
Figure 7. Temperature-dependent magnetization under ZFC−FC (zero field cooling−field cooling) conditions at applied field of 100−1000 Oe. (a) Effect of temperature on magnetization for iron oxide nanowire sample on alumina substrate prepared at 700 °C at 1000 Oe field strength. (b) Effect of temperature on magnetization for iron oxide nanowire sample on alumina prepared at 900 °C under 1000 Oe. (c) ZFC−FC curve for same sample as (a) under 100 Oe field strength.

not be diminished by the small size of the nanowires studied here. In fact, the Morin temperature has been found to decrease as particle size decreases in hematite samples, depressing this transition further away from the temperature shown in this figure. Publications reporting magnetic characterization of hematite nanowires and nanoparticles show only very weak ferromagnetic or paramagnetic behavior at room temperature, quite unlike our sample's hysteresis behavior. [23,41] Therefore, it is possible that the two compatible magnetic phases displayed in the graph shown in Figure 6a are not magnetite and hematite, but rather magnetite and the nanobelts of the ferrimagnetic ϵ-Fe_2O_3 phase. The figure shows an H_c value of about 4 kOe for this sample. This value is much less than the maximum reported room temperature coercivity of 20 kOe for ϵ-Fe_2O_3 nanoparticles. The decrease in coercivity may be due to interactions with the magnetite and hematite phases and the relatively low yield of ϵ-Fe_2O_3 compared to other phases in this sample. Since the reported 20 kOe value was obtained in samples containing IIA metal ions with much lower values reported for pure phase samples, [16] the absence of Mg may also provide some explanation for the lower coercivity demonstrated by this sample.

Figure 6b shows the M−H behavior of this sample at 5 K. It is clear that, at this low temperature, the hysteresis behavior disappears, producing a curve that looks much like a soft magnetic material. At 5 K, the magnetic response from the hard phase seen at room temperature disappears, so that the kinks

seen earlier disappear. This result indicates the presence of two phases with different temperature-dependent magnetic behaviors. This figure provides further evidence for the presence of magnetite and ϵ-Fe_2O_3 as magnetic phases in the sample. Previous reports on ϵ-Fe_2O_3 observe an unusual temperature dependence in which the coercivity decreases significantly below 100 K. This effect is described by Gich et al. to be due the Arrhenius nature of domain wall motion. The critical magnetic domain size may reduce to a value below the size of the nanostructure as T and therefore K (the reaction rate constant) decrease, causing an inhomogeneous state and loss of single-domain character. [18] The inset shows the expanded M−H loop, indicating magnetic saturation around 50 kOe.

Figure 6c,d shows similar data for the 900 °C sample. In this sample, the magnetic response from the softer phase has a greater influence on the overall hysteresis curve. Quantitative XRD measurements show that the hematite concentration in this sample is greater than that in the previous one, indicating that hematite nanostructures may be contributing to the change in magnetic response. Long nanobelts were also observed in large density on this sample, however, indicating that the influence of the ϵ-Fe_2O_3 phase cannot be ignored. The stronger soft magnetic response is further evident in Figure 6d, in which the area contained within the loop is observed to be smaller than that in the other sample.

It should be noted that further SQUID studies on small portions of samples shown in Figure 6 demonstrate typical hysteresis behavior, such as that of a soft magnetic material with small remnant magnetizations. It is very likely that these small portions contain a local phase domain such that the magnetic behavior again appears like that of a homogeneous group of ferrite nanowires. In these samples, SQUID measurements revealed saturation around 15 kOe when exposed to temperatures from 5 to 300 K.

The temperature dependence of the magnetization under ZFC−FC (zero field cooling−field cooling) conditions at 1000 Oe is shown in Figure 7a,b. The same sample shown in Figure 7a is measured again at 100 Oe, and the result is shown in Figure 7c. These figures show significant irreversibility from room temperature, with FC curves demonstrating Curie-like increasing. In Figure 7c, it is evident that the irreversibility occurs at 250 K. The magnetic field application direction should have little effect on these results since the nanowires are aligned only locally according to each grain, but globally they should appear as in random orientations. Strangely, these curves appear quite unlike those for other iron oxide nanostructures published in the literature, [3,18,25,30,32,41] and no Verwey transition point can be observed.

4. Conclusions

In this work, we report the first known PLD-assisted template-free growth of single-crystalline magnetite and hematite nanowires and nanobelts. We further report the success of the PLD method in the first known synthesis of long ϵ-Fe_2O_3 and Mg-stabilized ϵ-Fe_2O_3 nanowires and nanobelts. This technique offers many benefits over previous synthesis methods, including higher quality structures, higher density structures, greater spatial and size control, ability to grow complex structures, and no need for a template. In addition, the PLD method should allow synthesis of even more complex chemistries due to its ability to maintain the stoichiometry of the target material in the growing nanostructure. We include a primitive phase diagram for the synthesis of these structures and show how different variables affect the size, morphology, and phase of the grown

Growth of Ferrite Nanorods, Nanowires, and Nanobelts

J. Phys. Chem. B, Vol. 110, No. 43, 2006 **21679**

product. This information should be helpful both for those interested in utilizing this technique and for those hoping to further elucidate the underlying mechanisms behind VLS nanowire growth. We show high-density-aligned growth on polycrystalline alumina and report that the growth direction of the iron oxide nanowires can be controlled through use of different planes in single-crystalline substrates. SQUID measurements on these samples indicate novel and interesting magnetic properties which could be beneficial to many current and future technologies based on ferrite and magnetic materials.

References and Notes

(1) Hou, Y. L.; Yu, J. F.; Gao, S. *J. Mater. Chem.* **2003**, *13*, 1983.

(2) Wen, X. G.; Wang, S. H.; Ding, Y.; Wang, Z. L.; Yang, S. H. *J. Phys. Chem. B* **2005**, *109*, 215.

(3) Goya, G. F.; Berquo, T. S.; Fonseca, F. C.; Morales, M. P. *J. Appl. Phys.* **2003**, *94*, 3520.

(4) Pankhurst, Q. A.; Connolly, J.; Jones, S. K.; Dobson, J. *J. Phys. D: Appl. Phys.* **2003**, *36*, R167.

(5) Berry, C. C.; Curtis, A. S. G. *J. Phys. D: Appl. Phys.* **2003**, *36*, R198.

(6) Fang, B.; Wang, G. F.; Zhang, W. Z.; Li, M. G.; Kan, X. W. *Electroanalysis* **2005**, *17*, 744.

(7) Rossi, L. M.; Quach, A. D.; Rosenzweig, Z. *Anal. Bioanal. Chem.* **2004**, *380*, 606.

(8) Morishita, N.; Nakagami, H.; Morishita, R.; Takeda, S.; Mishima, F.; Terazono, B.; Nishijima, S.; Kaneda, Y.; Tanaka, N. *Biochem. Biophys. Res. Commun.* **2005**, *334*, 1121.

(9) Shinkai, M.; Yanase, M.; Suzuki, M.; Honda, H.; Wakabayashi, T.; Yoshida, J.; Kobayashi, T. *J. Magn. Magn. Mater.* **1999**, *194*, 176.

(10) Nitin, N.; LaConte, L. E. W.; Zurkiya, O.; Hu, X.; Bao, G. *J. Biol. Inorg. Chem.* **2004**, *9*, 706.

(11) Weissleder, R.; Elizondo, G.; Wittenberg, J.; Rabito, C. A.; Bengele, H. H.; Josephson, L. *Radiology* **1990**, *175*, 489.

(12) Ohmori, T.; Takahashi, H.; Mametsuka, H.; Suzuki, E. *Phys. Chem. Chem. Phys.* **2000**, *2*, 3519.

(13) Fried, T.; Shemer, G.; Markovich, G. *Adv. Mater.* **2001**, *13*, 1158.

(14) Gubin, S. P.; Spichkin, Y. I.; Yurkov, G. Y.; Tishin, A. M. *Russ. J. Inorg. Chem.* **2002**, *47*, S32.

(15) Chen, R. S.; Yung, E. K. N.; Ji, F.; Dou, W. B. *Int. J. Infrared Millimeter Waves* **2003**, *24*, 813.

(16) Jin, J.; Hashimoto, K.; Ohkoshi, S. *J. Mater. Chem.* **2005**, *15*, 1067.

(17) Ohkoshi, S.; Sakurai, S.; Jin, J.; Hashimoto, K. *J. Appl. Phys.* **2005**, *97*.

(18) Gich, M.; Roig, A.; Frontera, C.; Molins, E.; Sort, J.; Popovici, M.; Chouteau, G.; Marero, D. M. Y.; Nogues, J. *J. Appl. Phys.* **2005**, *98*.

(19) Tronc, E.; Chaneac, C.; Jolivet, J. P. *J. Solid State Chem.* **1998**, *139*, 93.

(20) Gich, M.; Frontera, C.; Roig, A.; Fontcuberta, J.; Molins, E.; Bellido, N.; Simon, C.; Fleta, C. *Nanotechnology* **2006**, *17*, 687.

(21) Berry, C. C. *J. Mater. Chem.* **2005**, *15*, 543.

(22) Hilger, I.; Andra, W.; Hergt, R.; Hiergeist, R.; Kaiser, W. A. *RoeFo, Fortschr. Geb. Roentgenstr.* **2005**, *177*, 507.

(23) Xu, Y. Y.; Rui, X. F.; Fu, Y. Y.; Zhang, H. *Chem. Phys. Lett.* **2005**, *410*, 36.

(24) Xue, D. S.; Zhang, L. Y.; Gao, C. X.; Xu, X. F.; Gui, A. B. *Chin. Phys. Lett.* **2003**, *21*, 733.

(25) Terrier, C.; Abid, M.; Arm, C.; Serrano-Guisan, L.; Gravier, L.; Ansermet, J.-Ph. *J. Appl. Phys.* **2005**, *98*, 086102.

(26) Wang, J.; Peng, Z.; Huang, Y.; Chen, Q. *J. Cryst. Growth* **2003**, *263*, 616.

(27) Gould, P. *Mater. Today* **2004**.

(28) Paine, T. O.; Mendelsohn, L. I.; Luborsky, F. E. *Phys. Rev.* **1955**, *100*, 1055.

(29) Zhang, D.; Zuquin, L.; Han, S.; Li, C.; Lei, B.; Stewart, M.; Tour, J.; Zhou, C. *Nano Lett.* **2005**, *5*, 2151.

(30) Liao, Z. M.; Li, Y. D.; Xu, J.; Zhang, J. M.; Xia, K.; Yu, D. P. *Nano Lett.* **2006**, *6*, 1087.

(31) Kelm, K.; Mader, W. *Z. Anorg. Allg. Chem.* **2005**, *631*, 2383.

(32) Yang, J. B.; Xu, H.; You, S. X.; Zhou, X. D.; Wang, C. S.; Yelon, W. B.; James, W. J. *J. Appl. Phys.* **2006**, *99*, 08Q507.

(33) Gao, P. X.; Ding, Y.; Wang, I. L. *Nano Lett.* **2003**, *3*, 1315.

(34) Wang, Z. L. *J. Phys.: Condens. Matter* **2004**, *16*, R829.

(35) Moore, D. F.; Ding, Y.; Wang, Z. L. *J. Am. Chem. Soc.* **2004**, *126*, 14372.

(36) Ding, Y.; Wang, X. D.; Wang, Z. L. *Chem. Phys. Lett.* **2004**, *398*, 32.

(37) Ma, C.; Wang, Z. L. *Adv. Mater.* **2005**, *17*, 2635.

(38) Ma, C.; Ding, Y.; Moore, D.; Wang, X. D.; Wang, Z. L. *J. Am. Chem. Soc.* **2004**, *126*, 708.

(39) Liu, Z.; Zhang, D.; Han, S.; Li, B.; Lei, C.; Lu, W.; Fang, J.; Zhou, C. *J. Am. Chem. Soc.* **2004**, *126*, 6.

(40) Reilly, A.; Allmond, C.; Watson, S.; Gammon, J.; Kim, J. G. *J. Appl. Phys.* **2003**, *93*, 3098.

(41) Bodker, F.; Hansen, M. F.; Koch, C. B.; Lefmann, K.; Morup, S. *Phys. Rev. B* **2000**, *61*, 6826.